Pd-Au nanostructured electrocatalysts with tunable compositions for formic acid oxidation

Elena Plaza-Mayoral[1], Inês Jordão Pereira[1], Kim Nicole Dalby[2], Kim Degn Jensen[1], Ib Chorkendorff[3], Hanne Falsig[2], Paula Sebastián-Pascual[1], María Escudero-Escribano[1]**

(1) Department of Chemistry, Center for High Entropy Alloy Catalysis, University of Copenhagen, Universitetsparken 5, 2100 Copenhagen, Denmark

(2) Haldor Topsøe A/S, Haldor Topsøe Allé 1, DK-2800 Kgs. Lyngby, Denmark

(3) Department of Physics, Surface Physics and Catalysis, Technical University of Denmark, Fysikvej, DK-2800 Lyngby, Denmark

*Corresponding authors:

E-mail: paula.pascual@chem.ku.dk

E-mail: maria.escudero@chem.ku.dk

KEYWORDS

Electrodeposition, electrocatalysis, formic acid oxidation, deep eutectic solvent, palladium-gold nanostructures.

ABSTRACT

The green transition requires new strategies to develop active and stable nanomaterials for energy conversion. We describe the preparation of Pd-Au bimetallic nanocatalysts using a surfactant-free electrodeposition method in a deep eutectic solvent (DES) and test their electrocatalytic performance for the formic acid oxidation reaction (FAOR). We use choline chloride plus urea DES to tune the composition of Pd and Au in the bimetallic nanostructures, as well as their morphology and active surface area. We measure the increase in the electrochemically active surface area (ECSA) of the prepared Pd-Au bimetallic surfaces by Cu underpotential deposition (UPD). Our results indicate a surface area increase of 5 to 12-fold compared to Pd and PdAu extended polycrystalline electrodes. We observe that the higher activity of Pd-Au nanostructures is principally due to its increased active area. Our results also reveal that Pd-Au nanostructures with *ca.* 50% of Pd and Au display the best activity and stability in relation to the Pd mass loading proving the synergy between Pd and Au in the bimetallic catalyst. We highlight that an in-depth analysis of the ECSA, as well as surface and electronic structure effects in bimetallic nanostructures, are crucial aspects for the rationalization of their catalytic properties.

TABLE OF CONTENTS GRAPHIC

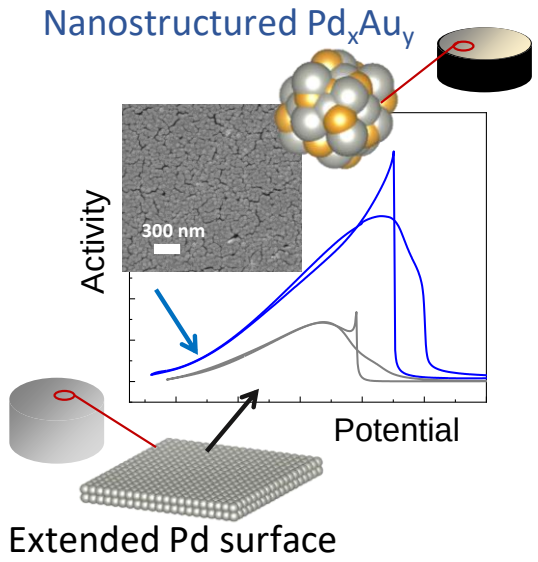

INTRODUCTION

The development of new and sustainable strategies for the controllable preparation of bimetallic nanostructured catalysts has gained attention in the past decade [1–3]. Compared to bulk materials, nanocatalysts often show improved electrocatalytic activity due to their high electrochemically active surface area (ECSA) combined with reduced loadings of noble and expensive metals. Additionally, their electrocatalytic properties can be tuned by tailoring the shape, size, morphology and composition [4]. Among other synthesis procedures, metal electrodeposition in deep eutectic solvents (DES) has emerged as a versatile, green and affordable alternative to prepare bimetallic and multi-metallic nanostructures [5]. DES are non-toxic solvents formed by the mixture between a quaternary ammonium salt and a neutral proton donor, and show wide potential limits and enough conductivity for metal electrodeposition [5–8]. Interestingly, they do not require the addition of surfactant agents to reduce the metal ions to its metallic form and calibrate the growth of the

nanostructures. These added surfactant-agents, typically used in colloidal nanoparticle syntheses, are difficult to remove and can deactivate the surface [9]. In contrast, the majority of DES are soluble in water and can be easily removed after the synthesis, allowing the preparation of clean and surface active nanostructures[10]. In recent years, some groups have investigated the electrodeposition of a few bimetallic nanostructures in DES, such as CuAu [11], PdPt or PdAg [12]. In our earlier work on Cu-Au bimetallic nanostructures prepared by co-electrodeposition in DES [11], we observed that the DES reduces the difference in the reduction potentials of Cu and Au, facilitating the co-deposition and formation of high surface area bimetallic Cu-Au with tunable composition. In this work, we prepare Pd-Au bimetallic nanostructures with tunable composition by electrodeposition in choline chloride: urea DES for the first time. This method provides an appealing and sustainable strategy to fabricate clean and active Pd-Au bimetallic nanostructures. We then test these bimetallic nanomaterials as electrocatalysts for the formic acid oxidation reaction in fuel cells.

The formic acid oxidation reaction (FAOR) have attracted interest since the 70s [13–15]. Fuel cells are promising energy conversion devices that convert the energy stored in the chemical bonds of a fuel into electricity. In a direct formic acid fuel cell (DFAFC), the oxidation of formic acid to carbon dioxide (CO_2) takes place at the anode, and the reduction of oxygen occurs at the cathode. The use of formic acid as a fuel has several benefits: it is soluble in water at room temperature, holds a high energy density and can be easily stored. These benefits make formic acid an excellent energy carrier to be integrated in a fuel cell if the generated CO_2 is captured and recycled to keep a carbon neutral-cycle [15–17]. The FAOR has been extensively investigated, particularly over Pd- and Pt-based materials, as they show relatively high performance [13,16]. Studies on Pt and Pd show that FAOR proceeds via two main mechanism paths: i) the complete oxidation of HCOOH to CO_2

through an active intermediate [16,18,19], i.e. the desired pathway; ii) a path involving the formation of poisoning species such as adsorbed CO [18,20], which suppresses the FAOR activity [19,21]. On Pt, the FAOR typically undergoes the two oxidation pathways in parallel [16,22–24]. In contrast, on Pd, it generally follows the first pathway, being fully oxidized to CO_2 [17,25–28]. Studies on different Pd facets and overlayers have revealed that FAOR on Pd is highly active and sensitive to both the catalyst structure and the electrolyte composition [29]. In particular, large Pd<100> domains in perchloric acid solutions display the best activities, while the <110> facets shows the lowest activity [30,31]. Increasing the amount of defect sites with <111> geometry reduces the activity of Pd, demonstrating the strong dependence of this reaction to the surface structure [30]. Despite the low CO poisoning effect, Pd still suffers from fast deactivation and degradation at high polarization conditions. Two main explanations of the Pd deactivation are: i) CO species are gradually formed and poison the surface [17,25,32–34], although the formation of CO from dehydration of HCOOH occurs at very slow rates [27]. ii) The adsorption of anions and oxygenated species (*e.g.* Pd-OH species, PdO and PdO_2) block and degrade the Pd surface [17,35]. To increase the stability of Pd and reduce CO poisoning over time, different strategies have been proposed. One strategy consists of decorating the Pd surface with adatoms such as SnO_2, which promotes the oxidation of CO-poisoning species enhancing the FAOR performance [25,36]. Alternatively, alloying or combining Pd with other elements such as Au can enhance the stability of Pd towards the FAOR [33,37]. In addition, the electrocatalytic activity of bimetallic materials can be typically enhanced with a combination of geometric and electronic effects [3,38]. Finding new methodologies to fabricate Pd-Au nanostructures with tailored composition and structure is an attractive alternative to tune the FAOR activity and stability.

The aim of this work is two-fold: 1) to establish a method to prepare Pd-Au nanostructures with tuned composition, morphology and size using a choline chloride: urea DES; 2) to perform an in-depth analysis of the critical parameters affecting the electrocatalytic performance of bimetallic Pd-Au nanostructures for the FAOR. We used flat polycrystalline Pd and PdAu extended electrode surfaces as benchmark electrodes for the reaction. To tune the nanostructure composition, we used bath-solutions with different concentrations of Pd and Au salts. Then we performed electrochemical deposition at moderate applied potentials to ensure controlled growth of the nanostructures. We observed that Pd-Au and Pd nanostructures displayed activities of *ca.* 3 to 7 times higher than PdAu(poly) and Pd(poly) extended surfaces. We found that differences in the activities and stability of the Pd-Au and Pd nanostructures towards the FAOR are not only related to the different compositions, but also to the surface structure and active surface areas.

EXPERIMENTAL SECTION

Preparation of the nanostructured Pd-Au deposits: The DES was prepared by mixing both choline chloride (ChCl, Across organics, 99%) and urea (Sigma-Aldrich, 99%) salts in a 1:2 molar ratio and under constant stirring at 40ºC. Different bath solutions were prepared with specific amounts of anhydrous $AuCl_3$ and $PdCl_2$ salts (Sigma-Aldrich, 99% purity) and dissolved in the DES under magnetic stirring, and heating conditions (T<60ºC) overnight. The metal-DES baths were then dried using either vacuum or an Ar stream for a few hours, to facilitate the co-deposition of the metals without the interference of the solvent and water-traces reduction [39].

The following bath solutions were prepared for the electrodeposition of the different metallic nanostructures: i) 0.1 M $AuCl_3$ + DES solution; ii) 0.14 M $PdCl_2$: 0.86M $AuCl_3$ + DES solution, *i.e*. Pd and Au 1:6 molar ratio; iii) 0.025 M $PdCl_2$: 0.075 M $AuCl_3$ + DES solution, *i.e.* Pd and Au

1:3 molar ratio; iv) 0.05 M $PdCl_2$: 0.05 M $AuCl_3$ + DES solution, *i.e*. Pd and Au 1:1 molar ratio; v) 0.075 M $PdCl_2$: 0.025 M $AuCl_3$ + DES, *i.e*. Pd and Au 3:1 molar ratio; vi) 0.05 M $PdCl_2$ + DES solution.

We carried out the metal electrodeposition in DES using a thermostatic small-volume (25 mL) three-electrode cell with two Au (or Pd for pure Pd deposition) wires acting as counter- and pseudo reference electrode. Potential values in the electrodeposition process, were referenced to the Ag|AgCl electrode scale. The temperature was kept at 70 ºC in all experiments carried out in DES to enhance the deposition rates and avoid the solvent co-reduction [39]. We conducted the depositions at constant potential using chronoamperometry technique until a specific charge was reached. We used a Biologic potentiostat and software to carefully monitor and calculate the integrated charge of the co-deposited Pd and Au nanostructures.

Surface pre-treatment and electrochemical measurements: The working electrodes utilized were: a glassy carbon (GC) disk as the substrate of the deposited nanostructures, a Au bead (prepared following the Cavalier method [40]), a polycrystalline Pd disk (from Mateck, 99.999% purity) and a PdAu alloy (Mateck, 99.999% purity; 5x3 mm). All of the working electrodes have a geometric area of 0.196 cm^2 except for the Au bead which is 0.208 cm^2. The preparation of the working electrodes consisted of polishing the GC electrode until mirror finish using water-based α-alumina powder of 0.3 µm and 0.05 µm coarseness (Struers). After polishing, the GC stub was sonicated in milli-Q (18.2 MΩcm, TOC<5 ppm) water for 1 minute, and dried with a nitrogen stream prior electrodeposition. The commercial Pd(poly) and PdAu(poly) electrodes were polished with α-alumina (0.05 µm) and then, sonicated with milli-Q water five times for 15 minutes. The polycrystalline electrodes were then electrochemically treated by cycling between [0.2 – 0.8] V

vs. RHE in 0.1 M $HClO_4$ electrolyte until stable cyclic voltammograms (CVs) manifested. The Au (bead) was pre-treated by flame-annealing and quenched in milli-Q water.

We carried out electrochemical measurements with the working electrodes in a meniscus configuration and in a three-electrode cell configuration using a Bio-Logic potentiostat. Cyclic voltammetry technique was used to assess the Cu UPD, CO stripping and FAOR in aqueous solution. The chronoamperometry technique was employed to perform the deposition of the Pd-Au nanostructures and to test their stability under FAOR conditions. A saturated calomel electrode (SCE) from Crison was used as a reference electrode and placed in a Lugging capillary. All results were converted to the reversible hydrogen electrode scale (RHE). The counter electrode was a gold wire for all Au containing samples and a Pt wire for pure Pd electrodes.

Cu underpotential deposition and determination of the ECSA: The Cu underpotential deposition solution was prepared using 10 mM $CuSO_4$ (Sigma-Aldrich, 99-100.5%) + 0.5 M H_2SO_4 (96%, Merck, Suprapur®). The calculation of the ECSA of the investigated samples relied on the separate integration of charge involved in the cathodic and anodic voltammetric curve of the Cu UPD CVs. Since the Cu UPD is a reversible process, an average of the cathodic and anodic charge values was calculated for each sample. These values were normalized with the geometric area of the working electrode to obtain the charge density of the electrode surfaces ($\mu C\ cm^{-2}$), which can be normalized to literature values [41–43].

Morphology and bulk composition analysis: Before the ex-situ morphological characterization, the samples were cleaned with milli-Q water at near 90 ºC, in order to remove residual DES from the surface. The morphology of the samples was analysed using the high-resolution Zeiss Gemini 500 field emission scanning electron microscope at Haldor Topsøe S/A. An Inlens and SE2 detector were used at low voltage (2 keV) to take high resolution images with the FE-SEM. Higher

voltages (15 keV) were used when collecting energy dispersive X-ray (EDS) data. EDS was performed using a Thermo Scientific UltraDry silicon drift detector and processed using Pathfinder Software. The EDS semi-quantitative analysis provided the weight percentages of Pd and Au in each sample, from which the total molar relation of Pd and Au in the deposited deposit was estimated. The loading of Pd and Au (mg cm^{-2}) in the nanostructures was calculated using the EDS data, giving the molar relation of Pd and Au in the sample, and from the charge circulated during the chronoamperometric deposition. We used the Faraday law: $Q = znF$, which relates the total amount of mols of deposited Pd and Au with the circulated charge. Q represents the circulated charge, z is the number of transferred electrons in the reduction of the ionic metals M^{z+}, n is number of moles of ions and, F is the Faraday constant (F= 96500 C/mol e^-).

X-ray photoelectron spectroscopy (XPS) analysis: XPS measurements were conducted by a Theta Probe instrument (Thermo Scientific) using an Al anode X-ray source (K_α line = 1,486.6 eV, pass energy 50 eV). The XPS base pressure was $<8.0\times10^{-9}$ mbar. Prior to the XPS measurements, the samples were sputtered (1keV, and 1.0 μA) with N6 Ar (1.1×10^{-7} mbar) for 15 min [44]. C 1*s*, O1*s*, Au 4*f*, Pd 3*d* and Au 4*d* peaks were measured near their expected positions in steps of 0.1 eV [45,46] in order to gain detailed insight on the chemical state and stoichiometry of the samples. The survey spectra is represented in the Supporting Information, Figure S4. Additionally, broad spectra surveys at 1 eV were obtained to identify potential sources of contamination (see supporting information). The CasaXPS software was used to process the data. The Au 4*d* peaks were fitted with a Gaussian-Lorentzian GL(100) shape with full width half maximum (FWHM) *ca.* 3.5 eV. The Pd 3*d* peaks were fitted a DS (0.1;100) (Doniach-Sunjic type [47]) peak shape with a maximum FWHM of 1.3 eV. Shirley type background was used for all instances.

CO stripping and FAOR measurements: Ultra-pure 0.1 M perchloric acid (Merck, Suprapur®, 99.995 % purity) was used when assessing base CVs and CO stripping. To perform the CO stripping measurements, the surface-electrodes were held at a potential value positioned in the capacitive region of each surface (between 0.46 and 0.52 V vs. RHE). Then, the solution was saturated with CO for 10 to 15 minutes to ensure that CO fully covers the surfaces. After that the solution was bubbled with Ar to remove the excess of CO in the cell. The adsorbed layer of CO was then oxidized going to a high potential value of 1.3 V vs. RHE. The CO stripping was monitored using CV at 20mV/s. Ultra-pure perchloric acid and formic acid (Sigma-Aldrich, ≥98% of purity) were used to prepare a 0.1 M $HClO_4$ + 0.2 M HCOOH employed for the for formic acid oxidation reaction. The FAOR was assessed by using CVs at 20 mV/s and the stability of the deposits was analysed by chronoamperometric technique. The potential of the anodic curves of the FAOR were *IR*-corrected. *IR* represents the ohmic drop, which is the electrode potential change induced by the current (*I*), though the electrolyte with resistance R_s. So the actual electrode potential is $E = E_{ap}\text{-}IR_s$, where Eap is the applied potential. The solution resistance R_s was measured by means impedance spectroscopy [48].

RESULTS AND DISCUSSION

Preparation and physical characterization of Pd-Au nanostructures

We have denoted samples prepared from the Pd and Au baths as follows along the manuscript: 1Pd:6Au, 1Pd:3Au, 1Pd:1Au and 3Pd:1Au. The number indicates the molar ratio of Pd and Au in the solution used to prepare the deposits. Description of the CVs, as well as the chronoamperometric curves of the Pd-Au deposition can be found in the Supplementary Information (S.I.). Co-electrodeposition of the Pd-Au bimetallic nanostructures on GC substrates

was performed by applying a moderate overpotential between -0.35 V and -0.40 V vs. Ag|AgCl (Figure S1). These applied potentials were selected to avoid fast growth of the deposit or overlapping with the solvent reduction, following a similar strategy to that in our previous work on the preparation of Cu-Au bimetallic nanostructures in DES [11]. At moderate applied overpotentials, we obtain bimetallic nanostructures homogeneously distributed on the surface. The morphological analysis of the Pd-Au bimetallic nanostructured electrodes from the four different Pd-Au bath solutions was assessed by FE-SEM. The depositions were performed at a selected low overpotential of -0.375 V vs. Ag | AgCl until reaching a charge of Q = -10 mC. The SEM image in Figure 1A shows that the 1Pd:6Au deposit produces sharp flower-shape nanoclusters of diameters larger than 300 nm, unlike Au nanoclusters which have a cauliflower-shape (Figure S2A) [49]. Figure 1B shows the morphology of the sample prepared from 1Pd:3Au solution. Similar to Figure 1A, flower-shaped nanoparticles (NPs) are formed but with a smaller diameter of *ca*. 100 nm. Increasing the Pd concentration as seen on the 1Pd:1Au sample, rounded NPs of around 100 nm are obtained instead. This concentration dependent morphology aspect of the NPs is clearly observable in Figure 1C. The size of these NPs decreases when the deposit is prepared from the 3Pd:1Au solution (Figure 1D). Very small NPs are formed coalescing and covering the substrate surface. The SEM analysis reveals that the progressive increase of the Pd in solution produces round and smaller nanoparticles similar to pure Pd (Figure S2B) [50]. The semi-quantitative EDS analysis of the abundance of the elements in the different Pd-Au samples (Figure S3) confirms the presence of both metals in the bimetallic nanostructures. It also shows evidence of the higher amount of Pd in the samples prepared from the Pd-concentrated bath solutions. Moreover, the EDS analysis (Figure S3A, B and C) indicates that the bulk molar ratio of the samples prepared from

the 1Pd:3Au, 1Pd:1Au and 3Pd:1Au solutions are approximately: Pd_1Au_3, PdAu and Pd_2Au_1 in line with the respective bath solution compositions.

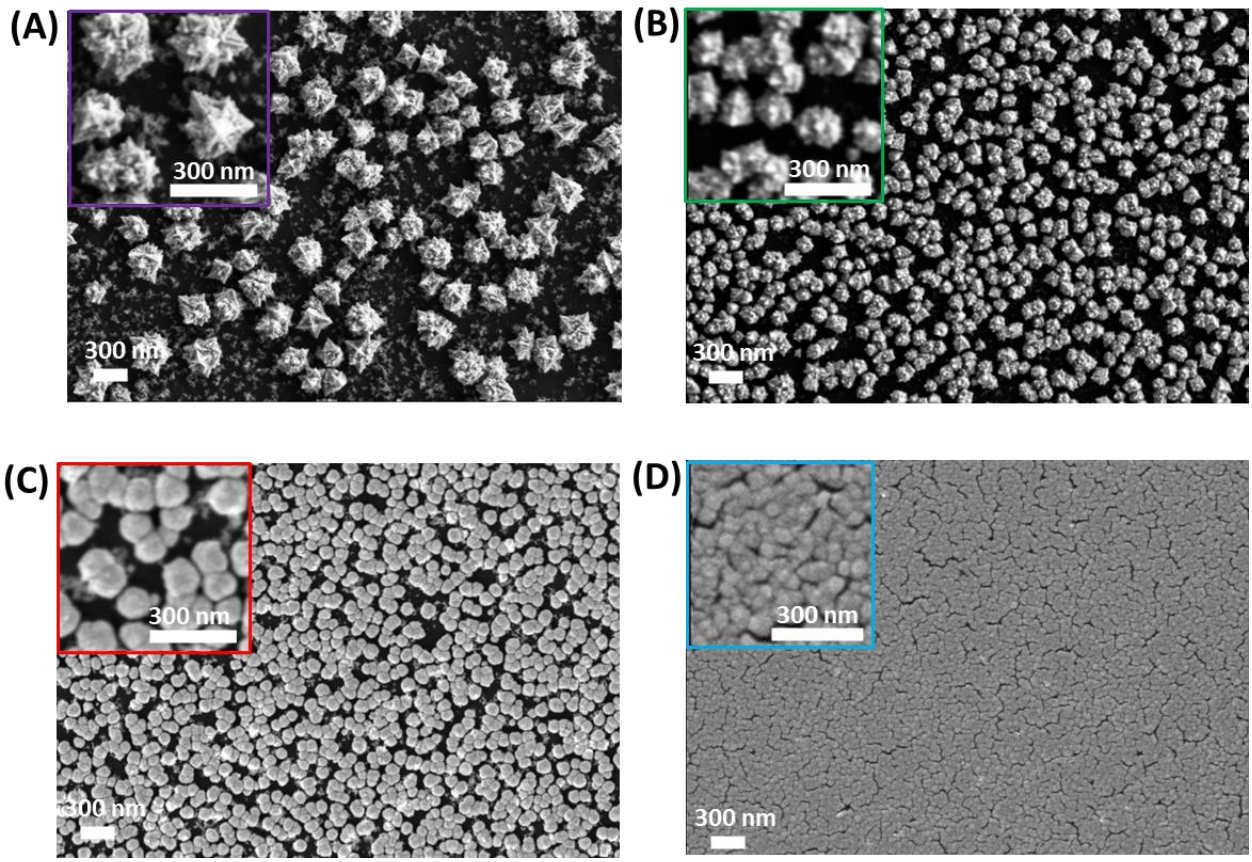

Figure 1: FE-SEM images of -10 mC deposits prepared at -0.375 V vs. Ag|AgCl from a molar ratio solution of (A) 1Pd:6Au; (B) 1Pd:3Au; (C) 1Au:1Pd; (D) 3Pd:1Au. All images have a horizontal field width (HFW) of 5 µm (the insets are a magnification of the main images with a factor of 2.7) and were taken at 2 keV.

To complement the EDS analysis, which provides semi-quantitative information of the bulk chemical composition of the nanostructures, we also carried out XPS measurements on 1Pd:3Au, 1Pd:1Au and 3Pd:1Au as-prepared nanostructured films, as well as the extended PdAu(poly) alloy.

Before performing the XPS analysis, the samples were slightly sputtered in order to remove the layer of contaminants on the top of the surface, as the samples have been stored in air for a long time. Figure 2 shows the XPS data for the four Pd-Au samples. The position of the advantageous carbon (C1*s*) was evaluated for each sample, and it remained constant at 284.5 eV [46], see Figure S5. We measured three observable peaks at binding energies of *ca.* 353 eV, 340 eV and 335 eV corresponding to Au 4$d_{3/2}$, Pd 3$d_{3/2}$ and the overlap of the Au 4$d_{5/2}$ and Pd 3$d_{5/2}$ peaks [51]. All four samples in Figure 2 show a peak, Au 4$d_{3/2}$, at binding energies between 353.1 eV to 352.9 eV, in line with previous reports [52]. The variation of the peak position for Au 4$d_{3/2}$ to lower binding energies is correlated to the increase of Pd content [53], see Figure S6. The same trend of chemical shift can be observed in the Au 4*f* peak, see Figure 2 [53]. The Pd 3$d_{3/2}$ position remains constant independently of the composition of the sample at 340.3 eV. The overlapping Au 4$d_{5/2}$ and Pd 3$d_{5/2}$ peaks give a good indication of the amount of palladium in the samples when conducting quantitative peak analysis. When the content of gold in the sample is higher, the Au4$d_{3/2}$ at *ca.* 352 eV peak, is more evident. On the other hand, when there is a higher Pd content, the Pd 3$d_{5/2}$ peak, at 335 eV adopts a sharp asymmetric shape characteristic of the Pd tail. We note that the Pd 3$d_{5/2}$ is less intense and broader in the 1Pd:3Au deposit (Figure 2B) compared to the PdAu(poly) sample (Figure 2A). However, we calculated that the 1Pd:3Au deposit has mainly the same composition of Pd as the PdAu(poly) alloy (Table S1). We attribute the observed Pd 3*d* peak changes to the variation in amount of defects and uncoordinated sites, which results in an increase of the FWHM and therefore broadening the peak [51,52].

To complement the interpretation of the Au 4*d* and Pd 3*d* XPS spectra, we show the Au 4*f* peaks on Figure 2. The Au 4$f_{7/2}$ is positioned at 83.9 eV for the 1Pd:3Au nanostructured film, whereas it is slightly shifted to 83.7 eV for the 3Pd:1Au as seen in Figure S6 [45,52]. The chemical shift can

be attributed to the presence of Pd and alloy formation that results in charge transfer between Au and Pd during the XPS excitation [53]. At 87 eV, there is the Pd 4*s* peak that we accounted for by fitting at this position a Gaussian-Laurentzian line shape with a FWHM of *ca.* 5eV. With the analysis of the Au 4*d*, Pd 3*d*, Au 4*f* and Pd 4*s* peaks we were able to confirm that the composition of the surface layers of the electrocatalyst roughly matched the composition of the DES bath solutions and the EDS. The 1Pd:3Au, 1Pd:1Au and 3Pd:1Au nanostructures showed elemental compositions of Pd of ~33%, ~60% and ~77% respectively (Table S1).

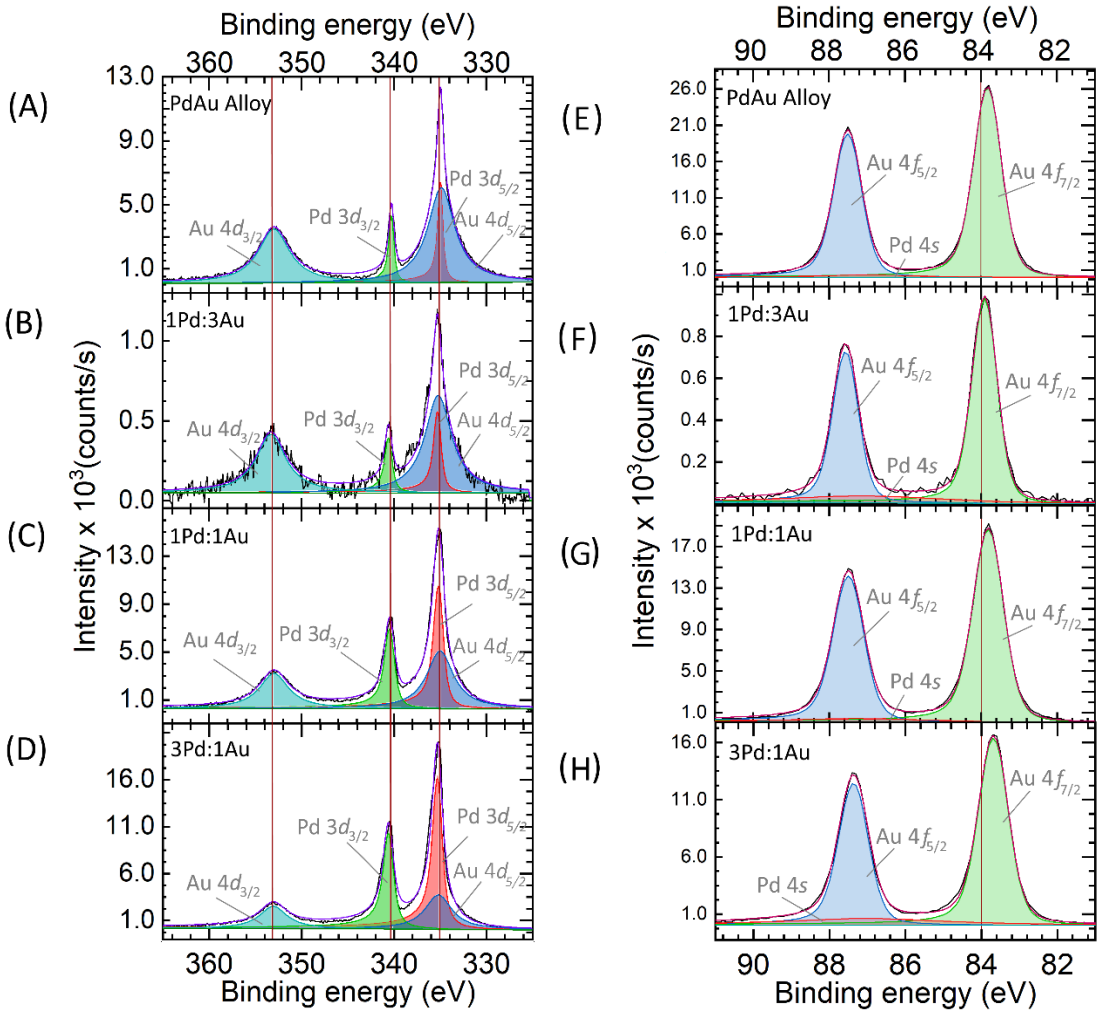

Figure 2: XPS spectra of PdAu(poly) and Pd-Au co-deposited nanostructures from 1Pd:3Au; 1Au:1Pd; and 3Pd:1Au bath solutions of (A-D) the Au 4*d* and Pd 3*d* peaks and, (E-H) the Au 4*f* and Pd 4*s* peaks. All spectra have been background subtracted (*Shirley* type background).

The active surface area accounts for the total number of reaction active site-positions per unit area of catalyst. Determination of the electrochemically active surface area (ECSA) is necessary to assess the intrinsic activity of the Pd-Au nanostructures towards the FAOR, affected by the specific geometry and electronic structure of the active sites [31]. The measured geometric activity is typically one or a few orders of magnitude higher than the intrinsic activity in nanomaterials, because the

high active surface areas are affected by the size, structure and distribution of the nanoparticles [1,3,43]. The increase in active area is given by the roughness factor *R*, which relates the ECSA with the catalyst geometric area as follows: $R=A_{ECSA}/A_{GA}$. To distinguish between size, structure and electronic effects on the FAOR on Pd-Au, we have probed the ECSA of the Pd-Au nanostructures by Cu UPD. Cu UPD accounts for the deposition of a submonolayer of Cu on the surface-catalysts, providing a voltametric profile which current intensity and shape is directly linked with the structure and number of active site positions. Cu UPD has been extensively used to characterize the structure of both Pd and Au surfaces, from extended single-crystalline and polycrystalline surfaces to nanoparticles [29,42,54,55]. By integrating the charge within the Cu UPD voltammetric profiles, it is possible to get insights on the surface active area of the prepared nanocatalysts [11].

Figure 3 shows the CVs of the Cu UPD on Pd-Au nanostructured films (blue, red and green lines) as well as the Cu UPD of the commercial extended PdAu alloy (dashed orange line). The Cu UPD profiles show characteristic features, which are a combination of the Cu UPD CVs of single Au and Pd surfaces (see Figure S7). The current density of the Cu UPD on the nanostructured films is substantially higher than on the commercial PdAu(poly) surface. Moreover, the Cu UPD progressively increases in intensity with the increase of the Pd content in the deposits, showing that the Pd-rich nanostructures present a larger ECSA. We ascribe these results to the smaller size of the Pd-rich nanostructures, which results in an increase of the number of active sites per unit area [56]. Table 1 summarizes the integrated values from the Cu UPD CVs, the estimated ECSA and the roughness factor R for the nanostructured deposits and the extended PdAu(poly) alloy. The charge value of the Cu UPD on an extended polycrystalline Pd electrode is *ca.* 401μC cm^{-2} [57–59], while for polycrystalline Au, Yang et al. reported a Cu UPD charge value of 445 μC cm^{-2} [60]. Considering the small difference charge between Au and Pd two surfaces, we have assumed that

the surface charge area of Pd-Au bimetallic surfaces with *R*=1 may range between 401 and 445 μC cm^{-2}. Using the AuPd(poly) as a benchmark we found a similar experimental integrated charge value of *ca.* 532 μC cm^{-2}. We also calculated a Cu UPD charge of *ca.* 455 μC cm^{-2} on the Pd(poly) extended surface, which lead a R of 1.2 ± 0.2 (Figure S7). The integrated charge values of the Cu UPD processes ranged between 2115 μC cm^{-2} for the 1Pd:3Au nanostructures and 4667 μC cm^{-2} for the 3Pd:1Au nanostructures, respectively. These results are clearly higher than the surface charge value of the PdAu(poly) alloy and Pd(poly). The prepared nanostructured deposits present high surface active areas and R between 5 and 11 (Table 1).

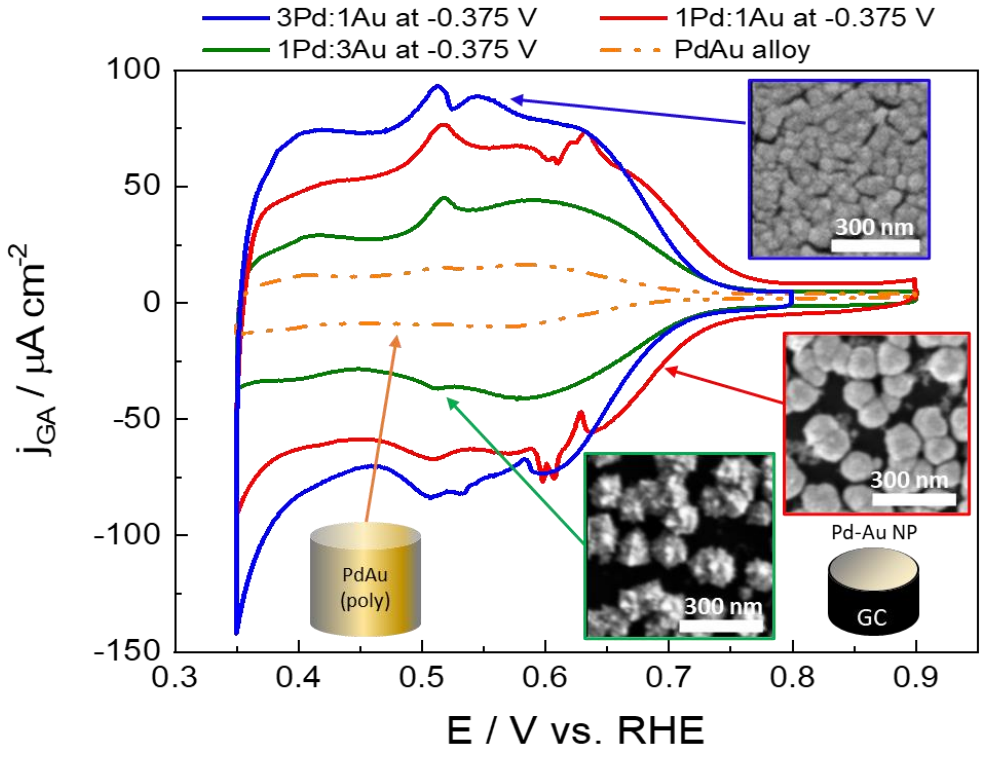

Figure 3: Voltammetric analysis of the Cu UPD in 0.5 M H_2SO_4 + 10 mM $CuSO_4$ at 5 mV/s for ~10 mC deposits prepared at -0.375 V vs. Ag|AgCl, and the PdAu alloy, normalized by the geometric area (GA). The bar in the SEM is equivalent to 300 nm.

Table 1. Calculated Cu UPD charges, ECSAs and roughness factors of the prepared samples of *Q* = -10 mC, and the PdAu(poly) electrode. For the calculations of the *R* we have used the following reference values: Q_{Pd}= 401 μC cm^{-2}, $Q_{Pd_3Au_1}$= 412 μC cm^{-2}, $Q_{Pd_1Au_3}$= 434 μC cm$^{-2,}$ and Q_{PdAu}= 423 μC cm^{-2} Q_{Au}=445 μC cm^{-2} [57,60]. These values have been calculated considering the Au:Pd molar ratio in each sample (determined by EDS and XPS) and the relative charge contribution of Pd and Au [57,60]. All potentials are vs. Ag|AgCl.

	Q/A_{ECSA} (μC cm^{-2})	A_{ECSA} (cm^2)	$R_{Cu\text{-}UPD}$
Pd at -0.2 V	4464 ± 274	2.18 ± 0.13	11.12 ± 0.68
3Pd:1Au at -0.375 V	4668 ± 195	2.22 ± 0.17	11.33 ± 0.47
1Pd:1Au at -0.375 V	3771± 232	1.75 ± 0.10	8.91 ± 0.55
1Pd:3Au at -0.375 V	2115 ± 195	0.96 ± 0.09	4.87 ± 0.45

CO oxidation and electrochemical behaviour of the Pd-Au nanostructures

As the formation of CO under FAOR conditions plays a key role in the activity and durability of the nanocatalysts, we started analysing the effect of the Pd and Au ratio on both the CO adsorption and oxidation. We investigated the voltammetric CO stripping, i.e., the oxidation of an adsorbed CO sub-monolayer on the Pd-Au surfaces to assess the poisoning effect of CO on the prepared catalysts [36,61,62]. Figure 4A illustrates the CO stripping curves on the different prepared bimetallic nanostructures, and figure 4B shows the CO stripping curves on the Pd(poly) and PdAu(poly) extended surfaces. The voltammetric currents are normalized by their calculated ECSA, using the Cu UPD technique, to better compare the Pd and PdAu nanostructures with the Pd(poly) and PdAu(poly) extended surfaces. The black line in figure 4A shows the CO stripping on the single Pd nanostructures, which displays a sharp and high oxidative current peak centred at 0.9 V vs.

RHE, similar to previous results in literature [27,30,63]. With the increase in Au content on the 3Pd:1Au, 1Pd:1Au and the 1Pd:3Au deposits (curves red, blue and green), the CO stripping current-maximum peak shifts to 0.92 V, 1.0 V and 1.1 V vs. RHE, respectively. Additionally, as the Au content increases, the CO stripping peaks become broader and lose symmetry, which demonstrates the effect of Au on the CO adsorption/oxidation [64]. Figure 4A shows the blank CVs of the Pd-Au nanostructures after stripping the CO adsorbed on the surface (second cycle, highlighted area). We have also plotted the blank CVs of Pd-Au nanostructures together in figure S8 for clarity. Figure 4A shows that Au also shifts the onset Pd surface oxidation in the Pd-Au deposits. In the cathodic scan the surface-oxide reduction peak shifts from 0.73 V vs. RHE (black curve, fig. 4A and S8) in pure Pd to 0.9 V vs. RHE in the 1Pd:3Au nanostructures (green curves, fig. 4A and S8). These results could be an indication that Au suppresses the adsorption of oxygenated species or changes the adsorption of hydroxide (OH) species, shifting both the CO-peaks and the Pd onset oxidation [33,64–68].

The integrated CO stripping charge values (normalized by the ECSA) of the Pd-Au samples in Table S2 can be used to qualitatively assess the impact that Au has on the CO adsorption and poisoning of Pd-Au. The integrated CO stripping charges were calculated after subtracting the contribution of the base CVs background to the total charge, mainly involving the surface oxidation and adsorption of OH groups [35] (highlighted area in Figure 4). The CO stripping normalized charge values for 3Pd:1Au and 1Pd:1Au (*ca.* 300-350 μC cm^{-2}) are slightly lower than the CO stripping charge value found for Pd nanostructures (387 μC cm^{-2}). These charge values are close to the reported value for pure polycrystalline Pd (317 μC cm^{-2}) [64], suggesting high CO coverages and that these samples contain an important surface Pd contribution. It is important to note that the integrated charge still contains two main overlapping contributions: i) the oxidation

of the adsorbed CO, ii) the adsorption of OH as the surface strips the CO. These two contributions cannot be accurately decoupled in this experiment, which limits the determination of changes in the amount of adsorbed CO on the Pd-Au nanostructures. However, the CO stripping charge value on the 1Pd:3Au sample decreases to 195 μC cm^{-2}. This result is a strong indication of a decrease of surface both CO coverage and adsorption, in the Au rich Pd-Au nanostructures [41,64,69,70].

Figure 4B shows the CO stripping on the Pd and PdAu(poly) extended surfaces. The CO stripping voltammetric profile on the Pd(poly) extended surface shows a sharp and intense oxidation peak at 0.95 V vs. RHE.[71] Notably, the blank CV recorded after the CO stripping, presents a prominent peak at 0.9 V that decreases in intensity by successively cycling between 0.2 V and 1.3 V vs RHE due to surface roughening and loosening of the ordering in long-terrace domains. A similar behaviour has been recorded on Pd single crystal electrodes[64]. The integrated CO stripping charge, after subtracting the charge of the formed Pd oxide, was 390 μQ cm^{-2}, similar to the charge reported for the prepared Pd nanostructures, and slightly higher than the value in literature (317 μC cm^{-2})[64]. We ascribe this difference in charge values to the difficulty in decoupling the Pd oxide formation from the CO oxidation process. The PdAu(poly) alloy shows a broader and less intense oxidation peak at more positive values of 1.1 V vs. RHE as in the case of the 1Pd:3Au deposit. Interestingly, the integrated charge for the CO stripping on the commercial PdAu alloy was 222 μC cm^{-2}, more similar to the 1Pd:3Au nanostructured deposit (195 μC cm^{-2}) than any of the other samples. Both electrodes have similar chemical compositions, as revealed by the XPS analysis, and have ca. 3 times more Au than Pd (Table S1). Results in figure 4B confirm that the prepared nanostructured electrodes display an electrochemical behaviour similar to the analogous extended surfaces. The results on the extended Pd(poly) and PdAu(poly) surfaces support that the changes in the CO-peak position, broadness and intensity are mainly due to an increase in the Au content at the surface. In

addition, Au also supresses the oxidation of Pd. These two aspects are highly relevant as they can affect the activity and stability of the Pd-Au bimetallic surfaces towards the FAOR.

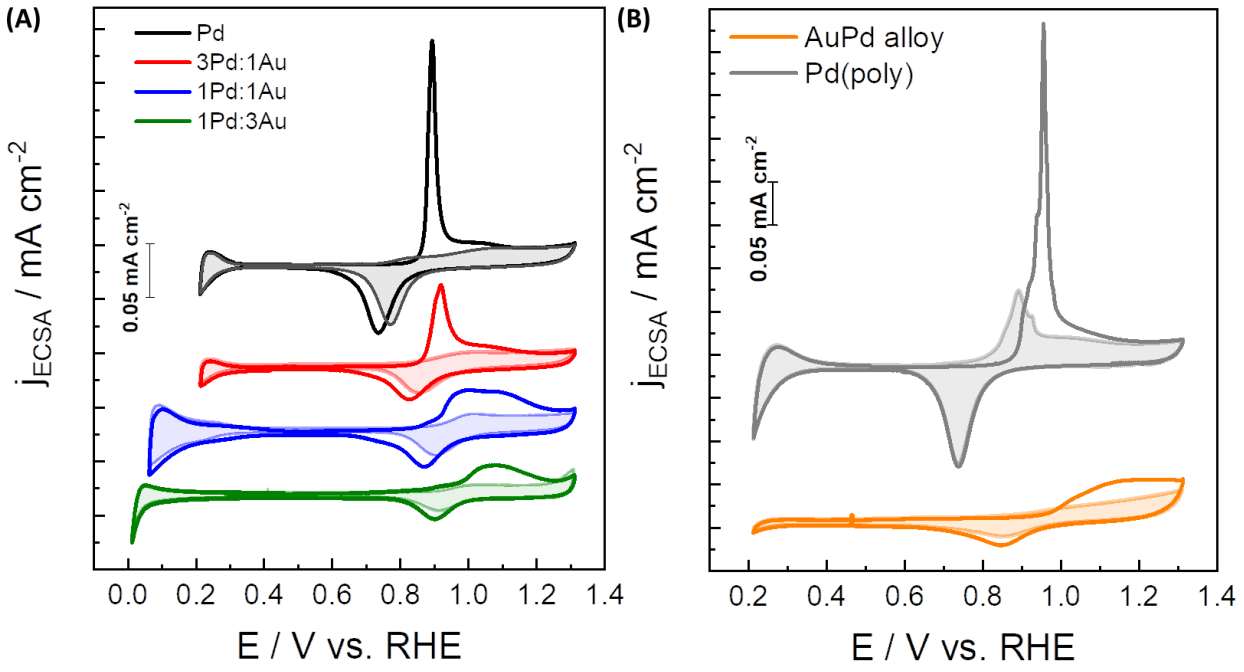

Figure 4: Voltammetric analysis of the CO stripping in 0.1 M $HClO_4$ at 20 mV/s for (A) -10 mC deposits from Pd at -0.2 V vs. Ag|AgCl, 3Pd:1Au, 1Pd:1Au and 1Pd:3Au, and (B) commercial Pd(poly) and PdAu(poly) alloy. All bimetallic Pd-Au deposits were prepared at -0.375 V vs. Ag|AgCl. The unfilled areas show the first cycle in which the CO adsorbed layer is stripped. The highlighted areas show the second cycle and correspond to the blank CVs of the Pd-Au bimetallic electrodes in 0.1 M $HClO_4$.

Formic acid oxidation on Pd and Pd-Au electrodes

We investigated the activity for the FAOR on the Pd-Au nanostructures in a 0.1 M $HClO_4$ electrolyte, as the adsorption of perchlorate anions on these electrode surfaces is negligible [61]. Figure 5A shows the voltammetric profiles of FAOR on the 1Pd:3Au and 1Pd:1Au deposits in a 0.2 M HCOOH + 0.1 M $HClO_4$ electrolyte. The red curve shows the FAOR on the 1Pd:1Au normalized by the geometric area (GA), which displays high current densities, revealing the

HCOOH oxidation. The current values increase while increasing the applied potential in the positive direction, until reaching a maximum value of 35 mA cm^{-2} at 0.8 V vs. RHE (the direction of the scan is indicated with arrows in figure 5A). Increasing the applied potential up to 1.35 V vs. RHE causes a sudden decrease of the activity due to the surface deactivation by the formation of surface oxide species. Consequently, when the scan is reversed, a voltammetric sharp peak appears at 0.99 V vs. RHE. This feature has been previously attributed to the fast activation of the FAOR after the reduction of the Pd or Pd-Au oxides [29]. Notably, currents from the negative and positive scans overlap, which suggests that the reaction mainly proceeds via direct HCOOH oxidation to CO_2 as supported by previous reports [25,29,34]. The FAOR activity of the 1Pd:1Au deposit is about one order of magnitude higher than that of the 1Pd:3Au deposit. Figure 5B shows the FAOR on the 1Pd:3Au and the extended PdAu(poly) alloy surfaces which have similar voltammetric shapes. Both surfaces display a voltammetric profile that is similar to the FAOR reported in pure gold catalysts [72], with two maximum current peaks in the anodic scan at 1.0 V and 1.5 V vs. RHE respectively. The 1Pd:3Au nanostructures is, however, four times more active than the PdAu(poly) alloy due to its higher ECSA. These results suggest that Pd-rich bimetallic surfaces enhance the FAOR activation[65]. In contrast, we observe that Au-rich nanostructures decreases the FAOR activities, noticeable by the poor performance when the Pd content is *ca.* 30% or less, as occurs in both the extended PdAu(poly) and 1Pd:3Au nanostructures [73].

Figure 5C shows the FAOR activities of the prepared 1Pd:1Au, 3Pd:1Au and Pd deposits plotted with the extended Pd(poly). The three nanostructured deposits display similar voltammetric profiles and maximum anodic current peaks above 35 mA cm^{-2} and at potential values of 0.8 V vs. RHE for Pd and 3Pd:1Au, and 0.85 V vs. RHE for 1Pd:1Au. In contrast, Pd(poly) (grey line) exhibits 2-3 times less intense geometric current densities than the nanostructured deposits.

Notably, the sharp FAOR spike recorded during the cathodic or negative scan shifts towards more positive values as the Au content increases. In particular, the sharp spike-feature at 0.8 V vs. RHE on both the Pd deposit and the Pd(poly) moves to 0.9 V vs. RHE in the 3Pd:1Au nanostructures and to 0.99 V vs. RHE in the 1Pd:1Au nanostructures. We assign the potential shift of the sharp spike feature to that Au reduces the adsorption of oxygenates species and shifts the Pd surface oxidation to more positive potential values. We also note that the potential of these FAOR CVs does not include the solution ohmic drop correction because it would obscure the voltammetric shape in the negative-going scan, attenuating the current of the sharp spike-feature [27]. However, we have represented in figure S9 the corresponding anodic or positive-going scans of the FAOR on Pd, 3Pd:1Au and 1Pd:Au with the ohmic drop correction: *E-iRs*. *Rs* is the solution resistant, *ca.* 40±3 Ω and *E* is the applied potential. After the ohmic drop correction, the maximum oxidation current peaks at *ca.* 35 mA cm^{-2} appeared at 0.52 V, 0.57 V and 0.6 V vs. RHE, respectively for Pd, 3Pd:1Au and 1Pd:1Au.

Figure 5D shows the current densities of the FAOR normalized by the ECSA. The aim is to assess how the relative content of Pd and Au in the sample affects the intrinsic activity of the FAOR. These results were compared with the FAOR on Pd(poly). The intrinsic activity of the extended Pd(poly) surface, at the maximum peak of the anodic scan, is clearly higher than the intrinsic activity of the Pd-Au and Pd deposits. Works performed by Hoshi et al. [30,74] on different Pd facets have shown that highly stepped <111>×<111> surfaces reduces the FAOR activity. We attribute the lower intrinsic activity of our nanostructures to a surface structure and NPs size effect, and that our nanostructures most likely contain high density of <111> defect-sites and undercoordinated sites [61]. The 1Pd:1Au nanostructures display the highest intrinsic current density among the three Pd and Pd-Au prepared nanostructures. The difference in their intrinsic currents, which is very

small, could be related to their different surface structures and roughness, or a small electronic effect of Au on Pd [61,67].

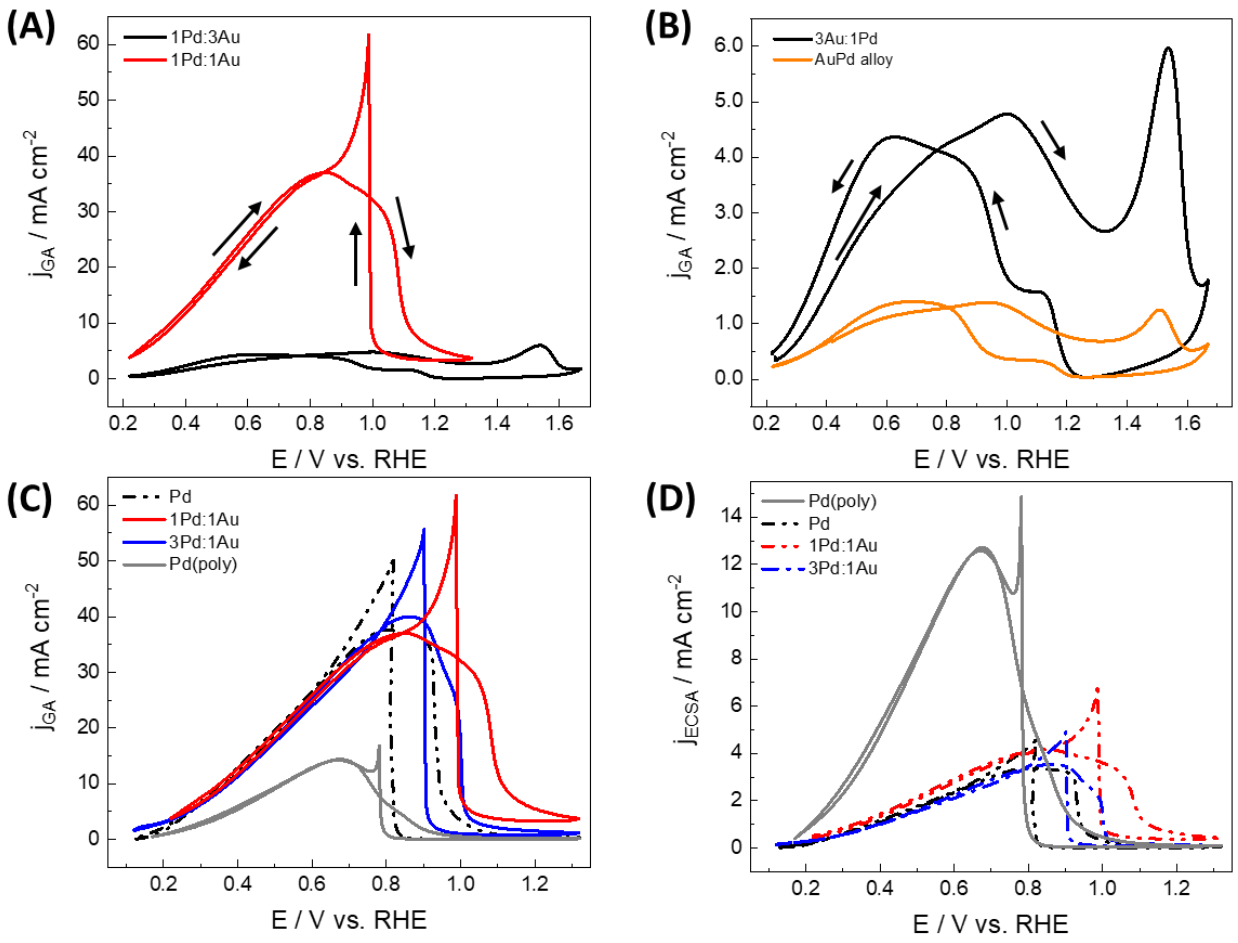

Figure 5: Voltammetric analysis in 0.1 M $HClO_4$ + 0.2 M HCOOH at 20 mV/s for **(A)** 1Pd :1Au (red line) and 1Pd :3Au (black line); **(B)** 1Pd:3Au in (A) compared to the commercial PdAu(poly) alloy response (orange line); **(C)** Pd deposit at -0.2 V vs. Ag|AgCl (black dashed line), 1Pd :1Au (red line) and 3Pd:1Au (blue line) against the geometric area compared with the Pd(poly) (grey line); and **(D)** all samples from (C) represented against the ECSA without ohmic-drop correction.

The results indicate that Pd is the active metal towards the FAOR, in line with previous reports [67,73]. To assess the effect of Au on the performance of Pd towards the FAOR, the analysis of the normalised activities of the different Pd-Au nanostructures per mass loadings of Pd is performed. This analysis provides insights on the maximum activities and stabilities achieved per milligram of Pd combined with specific amounts of Au. Figure 6A shows the activity of the prepared electrocatalysts for FAOR normalised by mass of Pd. The mass activity for the 1Pd:1Au nanostructures is above 3 A mg^{-1}_{Pd}, which is three times higher than the mass activity of the prepared Pd deposits (*ca.* 1 A mg^{-1}_{Pd}), consistent with previous results by Y. Suo et al. [65]. However, it is important to note that when the activities are normalized by the mass of both Pd and Au (Figure S10A), the electrocatalysts show equivalent activities of ca. 1 to 1.2 A $mg^{-1}_{(Pd+Au)}$. To clarify the influence of the Pd and Au composition on the stability of the bimetallic nanostructures, chronoamperometry measurements at a potential close to the current maximum peak were performed, *i.e.* at 0.72 V vs. RHE (Figure 6B). The surfaces suffer a deactivation after 20 minutes of performance, in good agreement with previous work [34,36,75]. The 1Pd:1Au bimetallic nanostructure displays higher stability than the 3Pd:1Au and pure Pd deposits showing mass activities about 150 mA mg^{-1}_{Pd} after two hours. In terms of activity normalized by the geometric area (j_{GA} vs. *t*, Figure S10B), the 1Pd:1Au only stands out by a small increase of activity, thereby still showing an important degree of surface deactivation [76]. Despite this strong surface deactivation, the presence of Au induces a slight improvement on the stability of the 1P:1Au towards the FAOR.

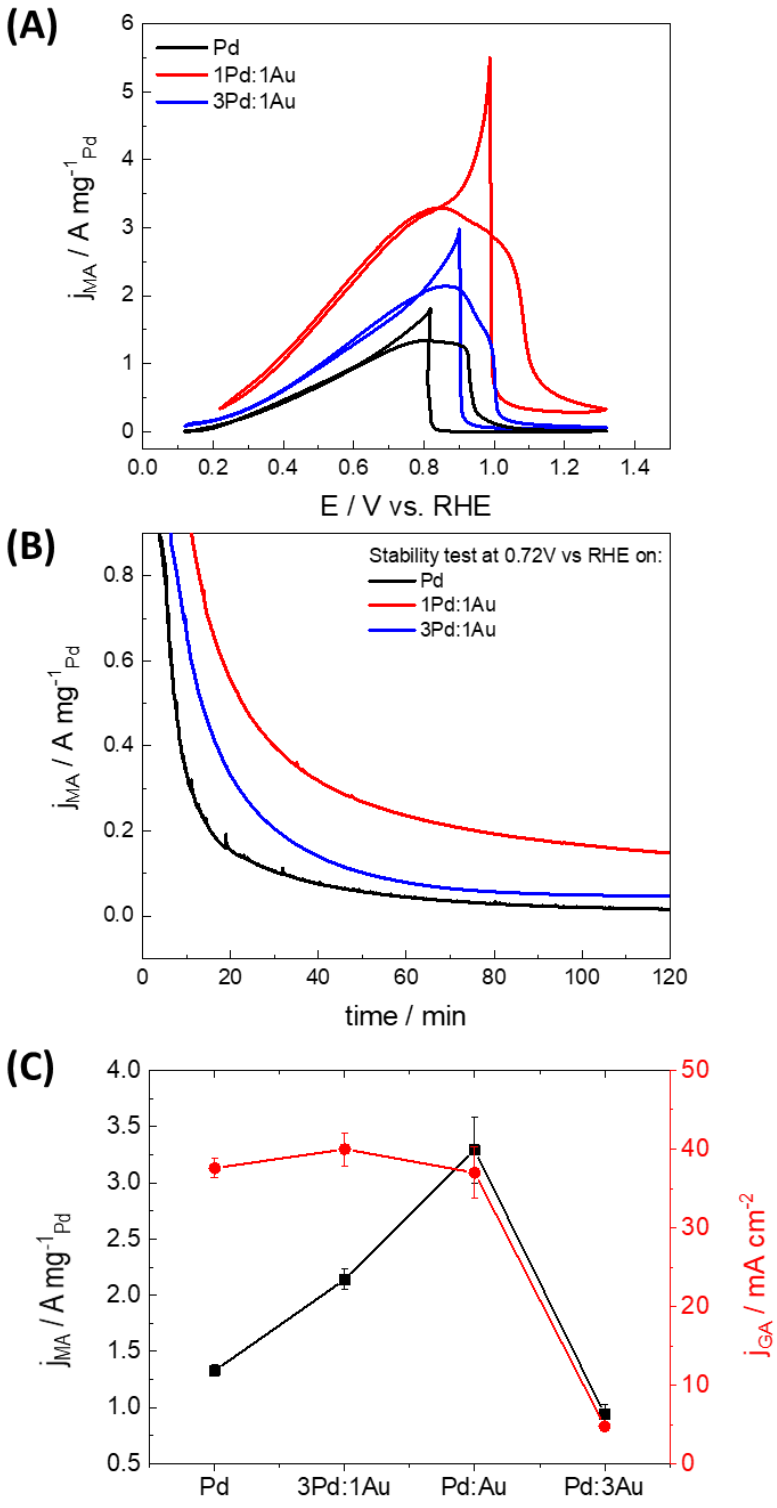

Figure 6: (A) Voltammetric analysis in 0.1 M $HClO_4$ + 0.2 M HCOOH at 20 mV/s showing the mass activity (normalised by mass of Pd, A mg^{-1}_{Pd}) of Pd deposit (black line), 1Pd :1Au (red line) and 3Pd:1Au (blue line) deposits. (B) Evolution of mass activity for the deposits from (A) after a

stability test consisting of two hours at 0.72 V vs RHE. (C) Representation of the geometric current density (black squares) and mass activity at the maximum current peak of the FAOR (red circles), for the four prepared nanostructures.

In Table S3, we summarize the effect of the Pd/Au ratio in the Pd-Au nanostructures on different key electrocatalytic parameters at the anodic peak in the FAOR curves (E_{peak} / V vs. RHE). These parameters are: activity normalized by geometric area of catalyst, intrinsic activity ($j_{GA,peak}$ and $j_{ECSA,\ peak}$ / mA cm^{-2}), and mass activity of Pd (mass activity / A mg^{-1}_{Pd}). Figure 6C shows the geometric and mass activities of the anodic peaks of the FAOR curves in the four nanostructures. Despite the Pd and Au loadings are different in Pd, 3Pd:1Au and 1Pd:1Au nanostructures, their FAOR activities are similar, while the activity considerably drops down in Pd:3Au. In contrast, we observe that a maximum activity per mass of Pd is reached with Pd:Au, i.e., Pd in Pd:Au is 3 times more active than Pd in pure Pd or in Pd:3Au nanostructures. Thus an optimum Pd mass loading is obtained for 1Pd:1Au. We also observe that Pd and Pd-rich Pd-Au nanostructures display higher FAOR activities than extended Pd(poly) principally due to their higher ECSA.

Discussion of the results

We observe that our 3Pd:1Au and Pd:Au nanostructures show both geometric and intrinsic activities that approach to pure Pd nanostructures, despite their different content in Pd and Au. Different studies have been carried out in the literature in order to rationalize the origin of the electrocatalytic activity of Pd:Au bimetallic catalysts toward the FAOR. Works performed by Lee et al. [73] have shown that the activity towards formic acid oxidation is improved on Pd_3Au NPs by applying a surface thermal treatment in a CO atmosphere. In this study, the CO resulted in the

segregation of Pd and increased its surface concentration in the catalyst, causing an increase of the FAOR activity. Other studies by Celorrio et al. [67] investigated how the thickness of the Pd layer in Au-Pd core-shell NPs affects the performance and stability FAOR. Samples with a thinner Pd layer (1.3 nm) showed low performance and similar to gold, whereas increasing the Pd layer thickness (9.9 nm) improved the FAOR performance. The authors proposed that the FAOR is influenced by strain effects of Au on the Pd shell. These studies highlight that Pd-Au nanocatalysts with high surface concentration of Pd exhibit more active FAOR. Regarding the stability of the nanostructures, it has been widely accepted that Pd deactivates over time due to the formation of CO, and that the presence of adsorbed OH groups is key to oxidize the adsorbed CO [36,77]. Celorrio et al. [67] proposed that thick Pd-Au NPs reduce the surface poisoning by CO due to the presence of adsorbed OH groups in these NPs, which also contributes to increase the FAOR. Interestingly, although OH groups are beneficial for CO removal, it has been also suggested that the increase in coverage of adsorbed oxygenated species can also block the surface, acting as poisoning species[62,65].

Our results reflect that Pd, 3Pd:1Au and 1Pd:1Au nanostructures are active towards the FAOR. In contrast, Au-rich 1Pd:3Au nanostructures present a drastic decrease in FAOR activity, in line with the above studies. We have also found that 1Pd:1Au, 3Pd:1Au and Pd are almost equally active despite their different Pd and Au loadings. CO stripping profiles suggest that Au is present in the superficial layers of 1Pd:1Au and 3Pd:1Au, as it induces a positive shift and broadening of the CO stripping peaks (figure 4A). These results indicate that Au possibly changes the poisoning strength of CO, or it modifies the surfaces coverages of OH in the Pd-Au samples [64,66,68,69]. Au also shifts the onset of the Pd surface oxidation to higher values, which indicates that Au affects the adsorption of oxygenated species [65]. Although Pd-rich surfaces are beneficial for active FAOR,

there must be different reasons that explain why Pd, 3Pd:1Au and 1Pd:1Au are almost equally active despite their different compositions. We attribute their similar performance to a combination of different structural and electronic effects, influencing the amount of actives sites per surface catalyst area and the intrinsic activity, respectively. Additionally, we assign the slightly higher stability of 1Pd:1Au under polarization conditions, to its superior ability in reducing poisoning effects. In this work, we show that nanostructures of Pd and Au with tuned morphology, composition and high active area for FAOR can be easily prepared in choline chloride plus urea DES.

CONCLUSIONS

We have shown, for the first time, the facile and clean fabrication of Pd-Au bimetallic nanostructures by co-electrodeposition in choline chloride: urea DES. These nanostructures present a 5 to 12-fold active area higher than Pd(poly) and PdAu(poly) extended surfaces. We use this method, consisting of the co-electrodeposition of Pd and Au in a DES, to tune the composition, morphology and size of Pd-Au bimetallic nanostructures for FAOR. By measuring the real electroactive area of the prepared nanostructures, we show that, overall, their high surface area is the main factor that explain its superior activity towards the FAOR compared to the PdAu(poly) and the Pd(poly) extended surfaces. Both Pd-Au and Pd nanostructures display similar geometric and intrinsic activities, and their intrinsic activities are lower than Pd(poly). This observation can be explained by the presence of more undercoordinated sites in the deposited nanostructures, which are intrinsically less active towards the FAOR than <100> and long terrace domains [29–31]. Interestingly, we observed that Au in the bimetallic structure only improves, slightly, its stability under reaction conditions, likely because it reduces the surface poisoning effects during the FAOR.

In conclusion, this work illustrates how the ECSA and chemical composition influence the electrocatalytic properties of Pd-Au nanocatalysts. An in-depth analysis of the ECSA, and the electronic and geometric structure is key to understand the origin of the enhanced electrocatalysis of bimetallic nanocatalysts towards the electrocatalytic reactions. Understanding and tuning these effects will be essential for the design of active and stable electrocatalysts for the FAOR in fuel cells. Our work also opens the door to the use of DES as non-toxic solvents to fabricate multimetallic nanostructures that combine a high active area with an enhanced electrocatalytic performance.

ORCID

Elena Plaza-Mayoral: 0000-0001-7208-7940

Inês Jordão Pereira: 0000-0002-6992-6472

Kim Nicole Dalby: 0000-0001-6048-3583

Kim Degn Jensen: 0000-0001-7466-8458

Ib Chorkendorff: 0000-0003-2738-0325

Hanne Falsig: 0000-0002-2474-4093

Paula Sebastián-Pascual: 0000-0001-7985-0750

María Escudero-Escribano: 0000-0002-6432-3015

Notes

The authors declare no competing financial interest.

ASSOCIATED CONTENT

Complementary CVs, CAs of Pd-Au electrodeposition in DES from 0.025 M $PdCl_2$: 0.075 M $AuCl_3$ + DES, 0.05 M $PdCl_2$: 0.05 M $AuCl_3$ + DES and 0.075 M $PdCl_2$: 0.025 M $AuCl_3$ + DES are explained. Additional FE-SEM and EDS analysis of single Au and Pd and, Pd-Au bimetallic samples from 1Pd:3Au, 1Pd:1Au and 3Pd:1Au are included. From the XPS analysis, the survey of a prepared nanostructure films, the position of the C 1*s* and O 1*s* peak for all the samples, the Au4$d_{3/2}$ and Au4$f_{7/2}$ peak position variation in the prepared nanostructures and, the calculated ratios of Pd and Au surface composition by the analysis of Au3*d* and Pd4*d* peaks are shown. The Cu UPD of a single Pd deposit and the polycrystalline Pd and Au with the PdAu alloy are also represented. The calculated charges from the CO stripping of the samples are summarized and the blank CVs of the samples in 0.1M $HClO_4$ are represented. The FAOR of the main samples with the potential corrected with the solution ohmic drop (E-iR) and versus the mass activity are shown for a better understanding. He same way, the stability test from the main three deposits (Pd, 3Pd:Au and, Pd:Au) versus the geometric area of the electrodes are shown. We finally summarize the effect of the Pd/Au ratio in the Pd-Au nanostructures on different key electrocatalytic parameters at the anodic peak in the FAOR curves.

AUTHOR INFORMATION

Corresponding Author

*E-mail: maria.escudero@chem.ku.dk

*E-mail: paula.pascual@chem.ku.dk

Author contributions

P.S.P. and M.E.E. conceived the original idea, planned the experiments and were in charge of the overall direction of this work. E.P.M. carried out the preparation of the Pd and PdAu

nanostructures and performed the electrochemical experiments, data analysis, and numerical calculations on Pd and PdAu nanostructures. I.J.P. and E.P.M performed the electrochemical experiments, data analysis and numerical calculations on polycrystalline PdAu and Pd extended surfaces. P.S.P. and M.E.E. supervised the electrochemical measurements and characterization. H.F. and K.N.D provided facilities for the SEM and EDS analysis, and discussion/guidance in the project conception. K.N.D. performed the SEM and EDS data acquisition and analysis. K.D.J. performed the XPS data acquisition and analysis with I.J.P. I.C. provided facilities for the XPS analysis and supervised the XPS work. E.P.M., I.J.P. and P.S.P. wrote the initial draft of the manuscript, which was edited and revised by K.N.D. and M.E.E. All the authors contributed to the interpretation of the results, provided critical feedback and helped shape the manuscript.

ACKNOWLEDGMENTS

We acknowledge support from the Danish National Research Foundation Center for High Entropy Alloy Catalysis (CHEAC, DNRF-149). This work was also supported by the Danish foundation through the DFF-Research Project1 (Thematic Research, green transition) grant with number: 0217-00213A. MEE gratefully acknowledges the Villum Foundation for financial support through a Villum Young Investigator Grant (project number: 19142).

REFERENCES

(1) Mistry, H.; Varela, A. S.; Kühl, S.; Strasser, P.; Cuenya, B. R. Nanostructured Electrocatalysts with Tunable Activity and Selectivity. *Nat. Rev. Mater.* **2016**, *1* (4), 16009. https://doi.org/10.1038/natrevmats.2016.9.

(2) Trogadas, P.; Ramani, V.; Strasser, P.; Fuller, T. F.; Coppens, M.-O. Hierarchically Structured Nanomaterials for Electrochemical Energy Conversion. *Angew. Chemie Int. Ed.* **2016**, *55* (1), 122–148. https://doi.org/https://doi.org/10.1002/anie.201506394.

(3) Sebastián-Pascual, P.; Jordão Pereira, I.; Escudero-Escribano, M. Tailored Electrocatalysts by Controlled Electrochemical Deposition and Surface Nanostructuring. *Chem. Commun.* **2020**, *56* (87), 13261–13272. https://doi.org/10.1039/D0CC06099B.

(4) Rodrigues, T. S.; Da Silva, A. G. M.; Camargo, P. H. C. Nanocatalysis by Noble Metal Nanoparticles: Controlled Synthesis for the Optimization and Understanding of Activities. *J. Mater. Chem. A* **2019**, *7* (11), 5857–5874. https://doi.org/10.1039/c9ta00074g.

(5) Wagle, D. V.; Zhao, H.; Baker, G. A. Deep Eutectic Solvents: Sustainable Media for Nanoscale and Functional Materials. *Acc. Chem. Res.* **2014**, *47* (8), 2299–2308. https://doi.org/10.1021/ar5000488.

(6) Bernasconi, R.; Panzeri, G.; Accogli, A.; Liberale, F.; Nobili, L.; Magagnin, L. Electrodeposition from Deep Eutectic Solvents. *Prog. Dev. Ion. Liq.* **2017**. https://doi.org/10.5772/64935.

(7) Zhang, Q.; De Oliveira Vigier, K.; Royer, S.; Jérôme, F. Deep Eutectic Solvents: Syntheses, Properties and Applications. *Chem. Soc. Rev.* **2012**, *41* (21), 7108–7146. https://doi.org/10.1039/c2cs35178a.

(8) Sebastian, P.; Giannotti, M. I.; Gómez, E.; Feliu, J. M. Surface Sensitive Nickel Electrodeposition in Deep Eutectic Solvent. *ACS Appl. Energy Mater.* **2018**, *1* (3), 1016–1028. https://doi.org/10.1021/acsaem.7b00177.

(9) Li, D.; Wang, C.; Tripkovic, D.; Sun, S.; Markovic, N. M.; Stamenkovic, V. R. Surfactant

Removal for Colloidal Nanoparticles from Solution Synthesis: The Effect on Catalytic Performance. *ACS Catal.* **2012**, *2* (7), 1358–1362. https://doi.org/10.1021/cs300219j.

(10) Smith, E. L.; Abbott, A. P.; Ryder, K. S. Deep Eutectic Solvents (DESs) and Their Applications. *Chem. Rev.* **2014**, *114* (21), 11060–11082. https://doi.org/10.1021/cr300162p.

(11) Plaza-Mayoral, E.; Sebastián-Pascual, P.; Dalby, K. N.; Jensen, K. D.; Chorkendorff, I.; Falsig, H.; Escudero-Escribano, M. Preparation of High Surface Area Cu-Au Bimetallic Nanostructured Materials by Co-Electrodeposition in a Deep Eutectic Solvent. *Electrochim. Acta* **2021**, *398*, 139309. https://doi.org/10.1016/j.electacta.2021.139309.

(12) Manolova, M.; Böck, R.; Scharf, I.; Mehner, T.; Lampke, T. Electrodeposition of Pd Alloys from Choline Chloride/Urea Deep Eutectic Solvents. *J. Alloys Compd.* **2021**, *855*, 157462. https://doi.org/https://doi.org/10.1016/j.jallcom.2020.157462.

(13) Capon, A.; Parsons, R. The Oxidation of Formic Acid on Noble Metal Electrodes: II. A Comparison of the Behaviour of Pure Electrodes. *J. Electroanal. Chem. Interfacial Electrochem.* **1973**, *44* (2), 239–254. https://doi.org/https://doi.org/10.1016/S0022-0728(73)80250-5.

(14) Rice, C.; Ha, S.; Masel, R. I.; Wieckowski, A. Catalysts for Direct Formic Acid Fuel Cells. *J. Power Sources* **2003**, *115* (2), 229–235. https://doi.org/https://doi.org/10.1016/S0378-7753(03)00026-0.

(15) Ma, Z.; Legrand, U.; Pahija, E.; Tavares, J. R.; Boffito, D. C. From CO2to Formic Acid Fuel Cells. *Ind. Eng. Chem. Res.* **2021**, *60* (2), 803–815. https://doi.org/10.1021/acs.iecr.0c04711.

(16) Fang, Z.; Chen, W. Recent Advances in Formic Acid Electro-Oxidation: From the Fundamental Mechanism to Electrocatalysts. *Nanoscale Adv.* **2021**, *3* (1), 94–105. https://doi.org/10.1039/d0na00803f.

(17) Shen, T.; Zhang, J.; Chen, K.; Deng, S.; Wang, D. Recent Progress of Palladium-Based Electrocatalysts for the Formic Acid Oxidation Reaction. *Energy and Fuels* **2020**, *34* (8), 9137–9153. https://doi.org/10.1021/acs.energyfuels.0c01820.

(18) Herrero, E.; Feliu, J. M. Understanding Formic Acid Oxidation Mechanism on Platinum Single Crystal Electrodes. *Curr. Opin. Electrochem.* **2018**, *9*, 145–150. https://doi.org/10.1016/j.coelec.2018.03.010.

(19) Betts, A.; Briega-Martos, V.; Cuesta, A.; Herrero, E. Adsorbed Formate Is the Last Common Intermediate in the Dual-Path Mechanism of the Electrooxidation of Formic Acid. *ACS Catal.* **2020**, *10* (15), 8120–8130. https://doi.org/10.1021/acscatal.0c00791.

(20) Cuesta, A.; Cabello, G.; Osawa, M.; Gutierrez, C. Mechanism of the Electrocatalytic Oxidation of Formic Acid on Metals. *ACS Catal.* **2012**, *2*, 728–738. https://doi.org/https://doi.org/10.1021/cs200661z.

(21) Perales-Rondón, J. V.; Ferre-Vilaplana, A.; Feliu, J. M.; Herrero, E. Oxidation Mechanism of Formic Acid on the Bismuth Adatom-Modified Pt(111) Surface. *J. Am. Chem. Soc.* **2014**, *136* (38), 13110–13113. https://doi.org/10.1021/ja505943h.

(22) Ferre-Vilaplana, A.; Perales-Rondón, J. V.; Buso-Rogero, C.; Feliu, J. M.; Herrero, E. Formic Acid Oxidation on Platinum Electrodes: A Detailed Mechanism Supported by Experiments and Calculations on Well-Defined Surfaces. *J. Mater. Chem. A* **2017**, *5* (41), 21773–21784. https://doi.org/10.1039/c7ta07116g.

(23) Cuesta, A.; Escudero, M.; Lanova, B.; Baltruschat, H. Cyclic Voltammetry, FTIRS, and DEMS Study of the Electrooxidation of Carbon Monoxide, Formic Acid, and Methanol on Cyanide-Modified Pt(111) Electrodes. *Langmuir* **2009**, *25* (11), 6500–6507. https://doi.org/10.1021/la8041154.

(24) Koper, M. T. M.; Lai, S. C. S.; Herrero, E. Mechanisms of the Oxidation of Carbon Monoxide and Small Organic Molecules at Metal Electrodes. *Fuel Cell Catal. A Surf. Sci. Approach* **2008**, 159–207. https://doi.org/10.1002/9780470463772.ch6.

(25) Shen, T.; Chen, S.; Zeng, R.; Gong, M.; Zhao, T.; Lu, Y.; Liu, X.; Xiao, D.; Yang, Y.; Hu, J.; Wang, D.; Xin, H. L.; Abruña, H. D. Tailoring the Antipoisoning Performance of Pd for Formic Acid Electrooxidation via an Ordered PdBi Intermetallic. *ACS Catal.* **2020**, *10* (17), 9977–9985. https://doi.org/10.1021/acscatal.0c01537.

(26) Rizo, R.; Roldan Cuenya, B. Shape-Controlled Nanoparticles as Anodic Catalysts in Low-Temperature Fuel Cells. *ACS Energy Lett.* **2019**, *4* (6), 1484–1495. https://doi.org/10.1021/acsenergylett.9b00565.

(27) Miyake, H.; Okada, T.; Samjeske, G.; Osawa, M. Formic Acid Electrooxidation on Pd in Acidic Solutions Studied by Surface-Enhanced Infrared Absorption Spectroscopy. *Phys. Chem. Chem. Phys.* **2008**, *10*, 3662–3669. https://doi.org/10.1039/B805955A.

(28) Chen, X.; Granda-Marulanda, L. P.; McCrum, I. T.; Koper, M. T. M. How Palladium Inhibits CO Poisoning during Electrocatalytic Formic Acid Oxidation and Carbon Dioxide Reduction. *Nat. Commun.* **2022**, *13* (1), 1–11. https://doi.org/10.1038/s41467-021-27793-5.

(29) Baldauf, M.; Kolb, D. M. Formic Acid Oxidation on Ultrathin Pd Films on Au(Hkl) and

Pt(Hkl) Electrodes. *J. Phys. Chem.* **1996**, *100* (27), 11375–11381. https://doi.org/10.1021/jp952859m.

(30) Hoshi, N.; Nakamura, M.; Kida, K. Structural Effects on the Oxidation of Formic Acid on the High Index Planes of Palladium. *Electrochem. commun.* **2007**, *9* (2), 279–282. https://doi.org/https://doi.org/10.1016/j.elecom.2006.09.023.

(31) Vidal-Iglesias, F. J.; Arán-Ais, R. M.; Solla-Gullón, J.; Garnier, E.; Herrero, E.; Aldaz, A.; Feliu, J. M. Shape-Dependent Electrocatalysis: Formic Acid Electrooxidation on Cubic Pd Nanoparticles. *Phys. Chem. Chem. Phys.* **2012**, *14* (29), 10258–10265. https://doi.org/10.1039/c2cp40992e.

(32) Jiang, K.; Zhang, H. X.; Zou, S.; Cai, W. Bin. Electrocatalysis of Formic Acid on Palladium and Platinum Surfaces: From Fundamental Mechanisms to Fuel Cell Applications. *Phys. Chem. Chem. Phys.* **2014**, *16* (38), 20360–20376. https://doi.org/10.1039/c4cp03151b.

(33) Tang, Y.; Zou, S. Formic Acid Oxidation on Pd Thin Film Coated Au Nanocrystals. *Surfaces* **2019**, *2* (2), 372–386. https://doi.org/10.3390/surfaces2020027.

(34) Wang, J.-Y.; Zhang, H.-X.; Jiang, K.; Cai, W.-B. From HCOOH to CO at Pd Electrodes: A Surface-Enhanced Infrared Spectroscopy Study. *J. Am. Chem. Soc.* **2011**, *133* (38), 14876–14879. https://doi.org/10.1021/ja205747j.

(35) Pizzutilo, E.; Geiger, S.; Freakley, S. J.; Mingers, A.; Cherevko, S.; Hutchings, G. J.; Mayrhofer, K. J. J. Palladium Electrodissolution from Model Surfaces and Nanoparticles. *Electrochim. Acta* **2017**, *229*, 467–477. https://doi.org/10.1016/j.electacta.2017.01.127.

(36) Rettenmaier, C.; Arán-Ais, R. M.; Timoshenko, J.; Rizo, R.; Jeon, H. S.; Kühl, S.; Chee,

S. W.; Bergmann, A.; Roldan Cuenya, B. Enhanced Formic Acid Oxidation over SnO2-Decorated Pd Nanocubes. *ACS Catal.* **2020**, *10* (24), 14540–14551. https://doi.org/10.1021/acscatal.0c03212.

(37) Zhu, X.; Guo, Q.; Sun, Y.; Chen, S.; Wang, J. Q.; Wu, M.; Fu, W.; Tang, Y.; Duan, X.; Chen, D.; Wan, Y. Optimising Surface d Charge of AuPd Nanoalloy Catalysts for Enhanced Catalytic Activity. *Nat. Commun.* **2019**, *10* (1), 1–11. https://doi.org/10.1038/s41467-019-09421-5.

(38) Maroun, F.; Ozanam, F.; Magnussen, O. M.; Behm, R. J. The Role of Atomic Ensembles in the Reactivity of Bimetallic Electrocatalysts. *Science (80-.).* **2001**, *293* (5536), 1811–1814. https://doi.org/10.1126/science.1061696.

(39) Sebastián, P.; Vallés, E.; Gómez, E. Copper Electrodeposition in a Deep Eutectic Solvent. First Stages Analysis Considering Cu(I) Stabilization in Chloride Media. *Electrochim. Acta* **2014**, *123* (I), 285–295. https://doi.org/10.1016/j.electacta.2014.01.062.

(40) Clavilier, J. The Role of Anion on the Electrochemical Behaviour of a 111 Platinum Surface; an Unusual Splitting of the Voltammogram in the Hydrogen Region. *J. Electroanal. Chem.* **1980**, *107* (1), 211–216. https://doi.org/10.1016/0368-1874(80)80077-3.

(41) Lukaszewski, M.; Soszko, M.; Czerwiński, A. Electrochemical Methods of Real Surface Area Determination of Noble Metal Electrodes - an Overview. *Int. J. Electrochem. Sci.* **2016**, *11* (6), 4442–4469. https://doi.org/10.20964/2016.06.71.

(42) Mayet, N.; Servat, K.; Kokoh, K. B.; Napporn, T. W. Probing the Surface of Noble Metals Electrochemically by Underpotential Deposition of Transition Metals. *Surfaces* **2019**, *2*

(2), 257–276. https://doi.org/10.3390/surfaces2020020.

(43) Herrero, E.; Buller, L. J.; Abruña, H. D. Underpotential Deposition at Single Crystal Surfaces of Au, Pt, Ag and Other Materials. *Chem. Rev.* **2001**, *101* (7), 1897–1930. https://doi.org/10.1021/cr9600363.

(44) Landa-Castro, M.; Sebastián, P.; Giannotti, M. I.; Serrà, A.; Gómez, E. Electrodeposition of Nanostructured Cobalt Films from a Deep Eutectic Solvent: Influence of the Substrate and Deposition Potential Range. *Electrochim. Acta* **2020**, *359*, 136928. https://doi.org/10.1016/j.electacta.2020.136928.

(45) Moulder, J. F. *Handbook of X-Ray Photoelectron Spectroscopy*; Chastain, J., Ed.; Physical Electronics Division, Perkin-Elmer Corporation, 1992.

(46) NIST. NIST Inorganic Crystal Structure Database (ICSD) SRD 3 https://icsd.nist.gov/.

(47) Doniach, S.; Sunjic, M. Many-Electron Singularity in X-Ray Photoemmision. *J. Phys. C Solid State Phys.* **1970**, *3*, 285–291. https://doi.org/https://doi.org/10.1088/0022-3719/3/2/010.

(48) Zamburlini, E.; Jensen, K. D.; Stephens, I. E. L.; Chorkendorff, I.; Escudero-Escribano, M. Benchmarking Pt and Pt-Lanthanide Sputtered Thin Films for Oxygen Electroreduction: Fabrication and Rotating Disk Electrode Measurements. *Electrochim. Acta* **2017**, *247*, 708–721. https://doi.org/https://doi.org/10.1016/j.electacta.2017.06.146.

(49) Wei, L.; Lu, B.; Sun, M.; Tian, N.; Zhou, Z.; Xu, B.; Zhao, X.; Sun, S. Overpotential-Dependent Shape Evolution of Gold Nanocrystals Grown in a Deep Eutectic Solvent. *Nano Res.* **2016**, *9* (11), 3547–3557. https://doi.org/10.1007/s12274-016-1236-1.

(50) Hammons, J. A.; Muselle, T.; Ustarroz, J.; Tzedaki, M.; Raes, M.; Hubin, A.; Terryn, H.

Stability, Assembly, and Particle/Solvent Interactions of Pd Nanoparticles Electrodeposited from a Deep Eutectic Solvent. *J. Phys. Chem. C* **2013**, *117* (27), 14381–14389. https://doi.org/10.1021/jp403739y.

(51) Levin, I. NIST Inorganic Crystal Structure Database. *NIST Public Data Repos.* **20218**, *1.0.0*. https://doi.org/10.18434/M32147.

(52) Rumble, J. R.; Bickham, D. M.; Powell, C. J. The NIST X-ray Photoelectron Spectroscopy Database. *Surf. Interface Anal.* **1992**, *19* (1–12), 241–246. https://doi.org/10.1002/sia.740190147.

(53) Nascente, P. A. P.; De Castro, S. G. C.; Landers, R.; Kleiman, G. G. *X-Ray Photoemission and Auger Energy Shifts in Some Gold-Palladium Alloys*; Vol. 8.

(54) Garnier, E.; Vidal-Iglesias, F. J.; Feliu, J. M.; Solla-Gullón, J. Surface Structure Characterization of Shape and Size Controlled Pd Nanoparticles by Cu UPD: A Quantitative Approach. *Front. Chem.* **2019**, *7* (July). https://doi.org/10.3389/fchem.2019.00527.

(55) Sebastián-Pascual, P.; Escudero-Escribano, M. Surface Characterization of Copper Electrocatalysts by Lead Underpotential Deposition. *J. Electroanal. Chem.* **2021**, *896* (May). https://doi.org/10.1016/j.jelechem.2021.115446.

(56) Narayan, N.; Meiyazhagan, A.; Vajtai, R. Metal Nanoparticles as Emerging Green Catalysts. *Materials (Basel).* **2019**, *12* (21), 1–34. https://doi.org/10.3390/ma12213602.

(57) Cuesta, A.; Kibler, L. A.; Kolb, D. M. Method to Prepare Single Crystal Electrodes of Reactive Metals: Application to Pd(Hkl). *J. Electroanal. Chem.* **1999**, *466* (2), 165–168. https://doi.org/10.1016/S0022-0728(99)00135-7.

(58) Huang, M.; Henry, J. B.; Fortgang, P.; Henig, J.; Plumeré, N.; Bandarenka, A. S. In Depth Analysis of Complex Interfacial Processes: In Situ Electrochemical Characterization of Deposition of Atomic Layers of Cu, Pb and Te on Pd Electrodes. *RSC Adv.* **2012**, *2* (29), 10994–11006. https://doi.org/10.1039/c2ra21558f.

(59) Chierchie, T.; Mayer, C. Voltammetric Study of the Underpotential Deposition of Copper on Polycrystalline and Single Crystal Palladium Surfaces. *Electrochim. Acta* **1988**, *33* (3), 341–345. https://doi.org/10.1016/0013-4686(88)85026-6.

(60) Yang, M.; Zhang, H.; Deng, Q. Understanding the Copper Underpotential Deposition Process at Strained Gold Surface. *Electrochem. commun.* **2017**, *82*, 125–128. https://doi.org/10.1016/j.elecom.2017.07.029.

(61) Solla-Gullon, J.; Vidal-Iglesias, F. J.; Lopez-Cudero, A.; Garnier, E.; Feliu, J. M.; Aldaz, A. Shape-Dependent Electrocatalysis: Methanol and Formic Acid Electrooxidation on Preferentially Oriented Pt Nanoparticles. *Phys. Chem. Chem. Phys.* **2008**, *10* (25), 3607–3608. https://doi.org/10.1039/b808799g.

(62) Baik, S. M.; Han, J.; Kim, J.; Kwon, Y. Effect of Deactivation and Reactivation of Palladium Anode Catalyst on Performance of Direct Formic Acid Fuel Cell (DFAFC). *Int. J. Hydrogen Energy* **2011**, *36* (22), 14719–14724. https://doi.org/10.1016/j.ijhydene.2011.04.181.

(63) Nogueira, J. A.; Varela, H. Voltage Oscillations in a Polymer Electrolyte Membrane Fuel Cell with Pd-Pt/C and Pd/C Anodes. *ChemistryOpen* **2017**, *6* (5), 629–636. https://doi.org/10.1002/open.201700098.

(64) Hara, M.; Linke, U.; Wandlowski, T. Preparation and Electrochemical Characterization of

Palladium Single Crystal Electrodes in 0.1 M H2SO4 and HClO4. Part I. Low-Index Phases. *Electrochim. Acta* **2007**, *52* (18), 5733–5748. https://doi.org/10.1016/j.electacta.2006.11.048.

(65) Suo, Y.; Hsing, I. M. Synthesis of Bimetallic PdAu Nanoparticles for Formic Acid Oxidation. *Electrochim. Acta* **2011**, *56* (5), 2174–2183. https://doi.org/10.1016/j.electacta.2010.12.037.

(66) Al-Odail, F. A.; Anastasopoulos, A.; Hayden, B. E. The Hydrogen Evolution Reaction and Hydrogen Oxidation Reaction on Thin Film PdAu Alloy Surfaces. *Phys. Chem. Chem. Phys.* **2010**, *12* (37), 11398–11406. https://doi.org/10.1039/b924656h.

(67) Celorrio, V.; Quaino, P. M.; Santos, E.; Flórez-Montaño, J.; Humphrey, J. J. L.; Guillén-Villafuerte, O.; Plana, D.; Lázaro, M. J.; Pastor, E.; Fermín, D. J. Strain Effects on the Oxidation of CO and HCOOH on Au–Pd Core–Shell Nanoparticles. *ACS Catal.* **2017**, *7* (3), 1673–1680. https://doi.org/10.1021/acscatal.6b03237.

(68) Blizanac, B. B.; Arenz, M.; Ross, P. N.; Markovic, N. M. Surface Electrochemistry of CO on Reconstructed Gold Single Crystal Surfaces Studied by Infrared Reflection Absorption Spectroscopy and Rotating Disk Electrode. *J. Am. Chem. Soc.* **2004**, *126* (32), 10130–10141. https://doi.org/10.1021/ja049038s.

(69) Bagger, A.; Ju, W.; Varela, A. S.; Strasser, P.; Rossmeisl, J. Electrochemical CO2Reduction: A Classification Problem. *ChemPhysChem* **2017**, *18* (22), 3266–3273. https://doi.org/10.1002/cphc.201700736.

(70) Morrow, B. H.; Resasco, D. E.; Striolo, A.; Nardelli, M. B. CO Adsorption on Noble Metal Clusters: Local Environment Effects. *J. Phys. Chem. C* **2011**, *115* (13), 5637–5647.

https://doi.org/10.1021/jp108763f.

(71) Fang, L. L.; Tao, Q.; Li, M. F.; Liao, L. W.; Chen, D.; Chen, Y. X. Determination of the Real Surface Area of Palladium Electrode. *Chinese J. Chem. Phys.* **2010**, *23* (5), 543–548. https://doi.org/10.1088/1674-0068/23/05/543-548.

(72) Beltramo, G. L.; Shubina, T. E.; Koper, M. T. M. Oxidation of Formic Acid and Carbon Monoxide on Gold Electrodes Studied by Surface-Enhanced Raman Spectroscopy and DFT. *ChemPhysChem* **2005**, *6* (12), 2597–2606. https://doi.org/10.1002/cphc.200500198.

(73) Lee, S. Y.; Jung, N.; Cho, J.; Park, H. Y.; Ryu, J.; Jang, I.; Kim, H. J.; Cho, E.; Park, Y. H.; Ham, H. C.; Jang, J. H.; Yoo, S. J. Surface-Rearranged Pd3Au/C Nanocatalysts by Using CO-Induced Segregation for Formic Acid Oxidation Reactions. *ACS Catal.* **2014**, *4* (8), 2402–2408. https://doi.org/10.1021/cs500227j.

(74) Hoshi, N.; Kida, K.; Nakamura, M.; Nakada, M.; Osada, K. Structural Effects of Electrochemical Oxidation of Formic Acid on Single Crystal Electrodes of Palladium. *J. Phys. Chem. B* **2006**, *110* (25), 12480–12484. https://doi.org/10.1021/jp0608372.

(75) Kucernak, A. R. J.; Fahy, K. F.; Sundaram, V. N. N. Facile Synthesis of Palladium Phosphide Electrocatalysts and Their Activity for the Hydrogen Oxidation, Hydrogen Evolutions, Oxygen Reduction and Formic Acid Oxidation Reactions. *Catal. Today* **2016**, *262*, 48–56. https://doi.org/10.1016/j.cattod.2015.09.031.

(76) Mikołajczuk, A.; Borodzinski, A.; Kedzierzawski, P.; Stobinski, L.; Mierzwa, B.; Dziura, R. Deactivation of Carbon Supported Palladium Catalyst in Direct Formic Acid Fuel Cell. *Appl. Surf. Sci.* **2011**, *257* (19), 8211–8214. https://doi.org/https://doi.org/10.1016/j.apsusc.2011.04.078.

(77) Ren, M.; Kang, Y.; He, W.; Zou, Z.; Xue, X.; Akins, D. L.; Yang, H.; Feng, S. Origin of Performance Degradation of Palladium-Based Direct Formic Acid Fuel Cells. *Appl. Catal. B Environ.* **2011**, *104* (1), 49–53. https://doi.org/https://doi.org/10.1016/j.apcatb.2011.02.029.